JOURNAL OF COMPUTATIONAL PHYSICS 38, 335–356 (1980)

Computation of Strongly Compressible Rotating Flows

I. HARADA

Energy Research Laboratory, Hitachi, Ltd.,
1168 Moriyama-cho, Hitachi, Ibaraki 316, Japan

Received May 17, 1979; revised November 27, 1979

A finite difference method is presented for investigating an axisymmetric continuum flow of a strongly compressible rotating gas in a gas centrifuge. Numerical investigations are made on both thermally and mechanically driven flows in an annulus to evaluate the method. The present method, based on the DuFort–Frankel/upwind scheme, is efficient for computations of these strongly compressible rotating flows. It is found that the thermally driven flow becomes weaker as the compressibility is increased. The viscous dissipation increases the gas temperature of the mechanically driven flow despite cooling by the expansion work.

1. INTRODUCTION

A fluid dynamics problem for a compressible rotating flow has arisen in uranium enrichment based on an ultracentrifugation process. This process uses the difference in the behaviour of two kinds of uranium isotope species in a strong centrifugal force field created inside a rapidly rotating cylinder of a gas centrifuge [1]. Centrifugal force causes the heavier isotope to move preferentially towards the pheriphery of the cylinder, producing a partial separation of the uranium isotopes in the radial direction. The success of the gas centrifuge depends on how to change the direction of enrichment from radial to axial by the induction of an axial flow in the rotation. This axial circulation flow is driven by imposing an appropriate temperature distribution on the solid boundaries of the cylinder (thermal drive) or by inserting a stationary object (scoop) near one end of the cylinder (mechanical drive). Both types of drives may also be combined (thermo-mechanical drive).

Theoretical investigations have been made by two different approaches [2–4]. One method is analytical and the other is numerical. With the former method, the compressible rotating flows were initially investigated on the basis of a classical approach [2]. Two typical approximations were presented, i.e., the long and the short cylinder approximations corresponding, respectively, to neglect of the end plates or that of the sidewall of the cylinder. However, these analyses were not appropriate from a gasdynamics viewpoint. Thermally and mechanically driven flows have also been investigated by using the boundary layer analyses [5–11] in which the counter-current flow is assumed as a small perturbation from the rigid body rotation. According to the results of the linear analysis, the flows in a gas centrifuge are essen-

0021-9991/80/150335-22$02.00/0

tially caused by the geostrophic wind (mechanically driven flow) or thermal wind (thermally driven flow) in the inviscid core. These winds in the inviscid core change into the Ekman layers on the end plates and into the $E^{1/4}$ layer or the $E^{1/3}$ layer [12] on the sidewall of the cylinder. These works are fruitful extensions of the theory of incompressible rotating flow [12–14] to the case of compressible rotating flow. The flow in a gas centrifuge is systematically analyzed by the boundary layer theory which is not used in the classical analysis. However, the range of applicability of the boundary layer theory is restricted to a local analysis when the compressibility effect becomes strong, or when the geometry of the gas centrifuge becomes complex.

In a numerical investigation, the motion of the gas is described by the equations of the continuum mechanics, i.e., the conservation of mass (continuity), momentum (Navier–Stokes equations) and energy together with a thermodynamics state law (perfect gas law). Numerical investigations have been made on the thermally driven flow of an incompressible fluid in a rotating cylinder [15] by using a finite difference method (FDM) and also on the thermally driven flow of a compressible gas in a rotating annulus [16] by using the Fourier spectral method. These works are not sufficient from the viewpoint of numerical investigations because either the compressibility [15] or nonlinearity [16] is neglected in the set of equations. Recently, three numerical methods have been developed [17–19]. The solution procedures are a FDM coupled with an overrelaxation method applied to the set of linearized equations [17], a FDM modified Newton algorithm applied to the set of nonlinear equations with no dissipation function [18], and a finite element method (FEM)/Newton–Raphson applied to the set of nonlinear equations with a dissipation function [19]. However, these methods need step-by-step iterations in the case of mixed boundary conditions such as for the thermo-mechanically driven flow (in which both the thermal and the mechanical drives coexist) or the nonlinear case such as for the flow which greatly deviates from rigid body rotation, because the convergency of these methods strongly depends on the initial guess of field variables. All these numerical studies except [15] treat steady flows.

The first aim of this paper is to establish a new method for numerical study of the flow in a gas centrifuge. This kind of study is a fundamental step towards understanding the separation process in a gas centrifuge. For this purpose, a finite difference method based on the DuFort–Frankel/upwind scheme is developed for solving the set of time-dependent nonlinear equations of strongly compressible rotating flow. The second aim is an investigation of the strongly compressible rotating flow such as the thermally and mechanically driven flows to which the boundary layer theory is not applicable.

2. Basic Equations of a Compressible Rotating Flow

Consider an axisymmetric continuum flow of a compressible rotating gas in an annulus. Figure 1 shows the rotating cylindrical coordinates fixed on the annulus. The radii of the inner and the outer cylinders are $r_a L$ and L, respectively, and the height

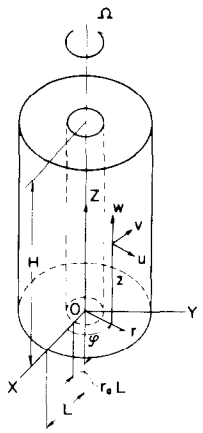

FIG. 1. A system of rotating cylindrical coordinates fixed on an annulus.

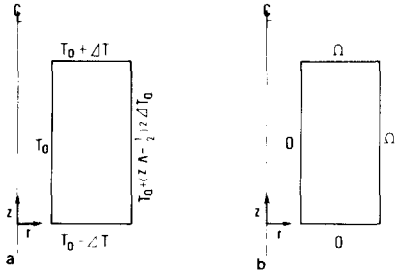

FIG. 2. Boundary conditions for (a) a thermally driven flow and (b) a mechanically driven flow. The annulus is rotating for a thermally driven flow and the uniform temperature T_0 is imposed on the annulus for a mechanically driven flow.

is $H(=AL)$, where A is an aspect ratio. Figure 2 illustrates the boundary conditions for thermally and mechanically driven flows. In the first problem (I), the annulus is rotating about the axis of rotation with a constant angular velocity Ω and the flow is driven by the temperature difference impulsively imposed on the surface; the top and bottom plates and the inner cylinder are changed from an initial temperature of T_0 to temperatures of $T_0+\Delta T$, $T_0-\Delta T$ and T_0, respectively, and the outer cylinder is changed to a temperature of the form $T_0+(z/A-1/2)\,2\Delta T$. Here coordinates (r, z) are scaled by the radius of the outer cylinder of L. In the second problem (II), the uniform temperature T_0 is imposed on the surface and the flow is mechanically driven by the angular velocity difference of the annulus; initially, both gas and the annulus are rotating with the angular velocity Ω and at temperature T_0, and then the bottom plate and the inner cylinder are stopped impulsively.

Let L, Ω^{-1}, ΩL, T_0 and ρ_0 be the characteristic length, time, velocity, temperature and density, respectively; then the continuity, the Navier–Stokes, the energy and the state equations scaled by $(L, \Omega^{-1}, \Omega L, T_0, \rho_0)$ are

$$\frac{D\rho}{D\tau} = 0, \tag{1}$$

$$\frac{D(\rho u)}{D\tau} + \rho r - \rho v\left(2 + \frac{v}{r}\right) = -\frac{1}{\gamma M^2}\frac{\partial p}{\partial r} + E\left[\mathscr{L}u + \frac{1}{3}\frac{\partial Q}{\partial r}\right], \tag{2}$$

$$\frac{D(\rho v)}{D\tau} + \rho u\left(2 + \frac{v}{r}\right) = E\mathscr{L}v. \tag{3}$$

$$\frac{D(\rho w)}{D\tau} = -\frac{1}{\gamma M^2}\frac{\partial p}{\partial z} + E\left[\nabla^2 w + \frac{1}{3}\frac{\partial Q}{\partial z}\right], \tag{4}$$

$$\frac{D(\rho T)}{D\tau} + (\gamma - 1)\rho T Q = \gamma E/\sigma_p \nabla^2 T + (\gamma - 1) M^2 E\Phi, \tag{5}$$

$$p = \rho T, \tag{6}$$

where

$$\nabla^2 = \frac{\partial^2}{\partial r^2} + \frac{1}{r}\frac{\partial}{\partial r} + \frac{\partial^2}{\partial z^2}, \qquad \mathscr{L} = \nabla^2 - \frac{1}{r^2},$$
$$Q = \nabla \cdot \mathbf{q} = \frac{1}{r}\frac{\partial}{\partial r}(ru) + \frac{\partial w}{\partial z}, \tag{7}$$

$$\Phi = 2\left[\left(\frac{\partial u}{\partial r}\right)^2 + \left(\frac{u}{r}\right)^2 + \left(\frac{\partial w}{\partial z}\right)^2\right] + \left(\frac{\partial v}{\partial r} - \frac{v}{r}\right)^2 + \left(\frac{\partial v}{\partial z}\right)^2 + \left(\frac{\partial w}{\partial r} + \frac{\partial u}{\partial z}\right)^2 - \frac{2}{3}Q^2. \tag{8}$$

In the above, $D(\ )/D\tau = \partial(\ )/\partial\tau + \nabla \cdot [(\ )\mathbf{q}]$ represents the Lagrangian derivative; u, v and w the radial, azimuthal and axial components of the fluid velocity $\mathbf{q} = (u, v, w)$ measured in a rotating cylindrical coordinates (r, φ, z), respectively; ρ the density; T the temperature; and p the pressure. The nondimensional numbers in the bove equations are defined by

$$\begin{aligned} E &= (\mu/\rho_0)/\Omega L^2 && \text{(Ekman number)},\\ M &= \Omega L/\sqrt{\gamma(R/m)\,T_0} && \text{(Mach number)},\\ \sigma_p &= (\mu C_p/k) && \text{(Prandtl number)},\\ \gamma &= C_p/C_v && \text{(Specific heat ratio)}, \end{aligned} \tag{9}$$

where μ is the viscosity; k the thermal conductivity; C_p and C_v the specific heats of constant pressure and volume, respectively; R the universal gas constant; and m the molecular weight of the gas.

The initial condition chosen here is the state of rigid body rotation given by

$$\begin{aligned} \rho_e &= \exp[(1/2)\,\gamma M^2(r^2-1)], \\ u = v = w = \theta &= 0, \end{aligned} \tag{10}$$

where $\theta = T - 1$ denotes the temperature difference from the characteristic value. The boundary conditions are as follows.

(I) Thermally driven flow:

$$\begin{aligned} &u = v = w = 0, && \text{at all boundaries,} \\ &\theta = -\varepsilon, && \text{at} \quad z = 0, \\ &\theta = \varepsilon, && \text{at} \quad z = \Lambda, \\ &\theta = \varepsilon(2z/\Lambda - 1), && \text{at} \quad r = 1, \\ &\theta = 0, && \text{at} \quad r = r_a. \end{aligned} \tag{11}$$

(II) Mechanically driven flow:

$$\begin{aligned} &u = w = \theta = 0, && \text{at all boundaries,} \\ &v = 0, && \text{at} \quad r = 1 \quad \text{and} \quad z = \Lambda, \\ &v = -r, && \text{at} \quad z = 0, \\ &v = -r_a, && \text{at} \quad r = r_a. \end{aligned} \tag{12}$$

To get information on the status of the unsteady motion, we introduce the kinetic energies and the average temperature of the gas defined by

$$\begin{aligned} E_u &= \langle \tfrac{1}{2}\rho u^2 \rangle, \\ E_v &= \langle \tfrac{1}{2}\rho v^2 \rangle, \\ E_w &= \langle \tfrac{1}{2}\rho w^2 \rangle, \\ E_t &= E_u + E_v + E_w, \\ \theta &= \langle T - 1 \rangle / \langle 1 \rangle, \end{aligned} \tag{13}$$

where $\langle\ \rangle$ denotes the volume integral over the r–z cross section of the annulus defined by

$$\langle \phi \rangle = 2\,\pi \int_{r_a}^{1} \int_{0}^{\Lambda} \phi r\, dr\, dz.$$

3. Finite Difference Method Based on Conservation Laws

The finite difference method developed in this paper is based on conservation laws. There are two problems to be solved before deriving the finite difference equations. First is the mathematical expressions from which we start. We used the primitive form of equations which describe the conservations of mass, momentum and energy in the torous volume $(2\pi)\, r\, dr\, dz$ instead of Eqs. (1)–(6); these are derived by the replacement of ρ by $\hat{\rho} = \rho r$ in Eqs. (1)–(6). Here, the convective term is transformed from cylindrical into Cartesian coordinates. Second is the grid arrangement on the computational domain which is divided into rectangular cells (i, j) or sides Δr_i and Δz_j in the radial and axial directions, respectively. Figure 3 shows the staggered grids in which the physical variables are defined at the different grid points to conserve the mass in the cell volume; the density ρ, the pressure p, and the temperature T are defined at the center of each cell; the radial and axial components of the (mass) velocity $u(\rho u)$ and $w(\rho w)$ are defined at the midpoints of the radial and axial edges of the cell, respectively; and the azimuthal component of the (mass) velocity $v(\rho v)$ is defined at the same point as $u(\rho u)$. It should be noted that the mass transfer is completely satisfied in the cell volume by this Cartesian form of the convective term and by the staggered grids on the computational domain.

An explicit scheme of the DuFort–Frankel leapfrog type of the second ordered accuracy is used for both time derivative and diffusion terms. The centered difference scheme of the second ordered accuracy is used for all the space derivatives except the convective term. The second upwind scheme [20] or donor cell method [21] is used for the convective term to ensure the numerical stability (see Table I). The second upwind scheme retains something of the second ordered accuracy of the centered space derivatives as is discussed in [20]. Hence, the present finite difference is essentially the second ordered accuracy for both time and space.

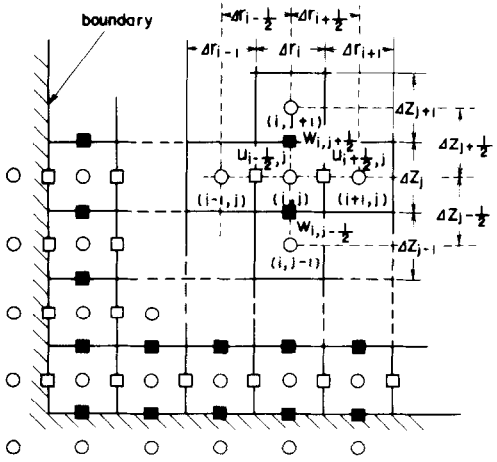

FIG. 3. An arrangement of grid point; ○, ρ and T are defined at cell center; □, u (or ρu) and v (or ρv); ■, w (or ρw).

TABLE I

Upwind Scheme of $\partial(u\phi)/\partial x$

	Signs of velocities	$\partial(u\phi)/\partial x$	ϕ_{i-1} ϕ_i ϕ_{i+1}
(a)	$u_{i-1/2}, u_{i+1/2} > 0,$	$\frac{1}{\Delta x}\{u_{i+1/2}\phi_i - u_{i-1/2}\phi_{i-1}\}$	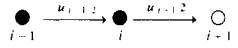
(b)	$u_{i-1/2}, u_{i+1/2} > 0,$	$\frac{1}{\Delta x}\{u_{i+1/2}\phi_{i+1} - u_{i-1/2}\phi_i\}$	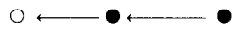
(c)	$u_{i-1/2} > 0, u_{i+1/2} < 0,$	$\frac{1}{\Delta x}\{u_{i+1/2}\phi_{i+1} - u_{i-1/2}\phi_{i-1}\}$	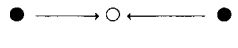
(d)	$u_{i-1/2} < 0, u_{i+1/2} > 0,$	$\frac{1}{\Delta x}\{u_{i+1/2} - u_{i-1/2}\}\phi_i$	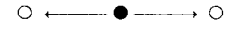

Using the schemes mentioned above, we obtain the finite difference equations as follows (dropping the caret from ρ):

$$(\rho^{n+1} - \rho^{n-1})/2\Delta\tau = -[\delta_r(\rho u)^{n+1} + \delta_z(\rho w)^{n+1}], \tag{14}$$

$$\begin{aligned}[(\rho u)^{n+1} - (\rho u)^{n-1}]/2\Delta\tau &= -[\delta_r(\rho uu) + \delta_z(\rho wu)]^n + \left[\rho\left(r + \left(2 + \frac{v}{r}\right)\right)\right]^n - \frac{1}{\gamma M^2} r\,\delta_r p^n \\ &\quad + Er\left[\frac{4}{3}\left(\delta_r\delta_r u^{\bar{n}} + \delta_r\left(\frac{u}{r}\right)^n\right) + \delta_z\delta_z u^{\bar{n}} + \frac{1}{3}\delta_r\delta_z w^n\right],\end{aligned} \tag{15}$$

$$\begin{aligned}[(\rho v)^{n+1} - (\rho v)^{n-1}]/2\Delta\tau &= -[\delta_r(\rho uv) + \delta_z(\rho wv)]^n - \left[\rho u\left(2 + \frac{v}{r}\right)\right]^n \\ &\quad + Er\left[\delta_r\delta_r v^{\bar{n}} + \delta_r\left(\frac{v}{r}\right)^n + \delta_z\delta_z \bar{v}^n\right],\end{aligned} \tag{16}$$

$$\begin{aligned}[(\rho w)^{n+1} - (\rho w)^{n-1}]/2\Delta\tau &= -[\delta_r(\rho uw) + \delta_z(\rho ww)]^n - \frac{1}{\gamma M^2} r\,\delta_z p^n \\ &\quad + Er\left[\delta_r\delta_r w^{\bar{n}} + \frac{1}{r}\delta_r w^n + \frac{4}{3}\delta_z\delta_z w^{\bar{n}} + \frac{1}{3}\delta_z\left(\frac{1}{r}\delta_r u^n\right)\right],\end{aligned} \tag{17}$$

$$[(\rho T)^{n+1} - (\rho T)^{n-1}]/2\Delta\tau$$
$$= -[\delta_r(\rho u)^{n+1} T^n + \delta_z(\rho w)^{n+1} T^n] - (\gamma - 1)(\rho T)^{n+1} Q^n$$
$$+ \gamma E/\sigma_p r[\delta_r \delta_r T^{\bar{n}} + (1/r)\,\delta_r T^n + \delta_z \delta_z T^{\bar{n}}] + (\gamma - 1)\,\gamma M^2 E r \Phi^n, \quad (18)$$
$$p^{n+1} = (\rho T)^{n+1}/r, \quad (19)$$

where

$$Q = (1/r)\,\delta_r(ru) + \delta_z w,$$
$$\Phi = 2[(\delta_r u)^2 + (u/r)^2 + (\delta_z w)^2] + (\delta_r v - v/r)^2 \quad (20)$$
$$+ (\delta_z v)^2 + (\delta_r w + \delta_z u)^2 - \tfrac{2}{3}Q^2.$$

In the above equations, the differences are defined by

$$\delta_x \phi_i = (\phi_{i+1/2} - \phi_{i-1/2})/\Delta x_i, \quad (21)$$
$$\delta_x \delta_x \phi_i^{\bar{n}} = [(\phi_{i+1} - \bar{\phi}_i)/\Delta x_{i+1/2} - (\bar{\phi}_i - \phi_{i-1})/\Delta x_{i-1/2}]^n/2\Delta x_i, \quad (22)$$

with

$$\bar{\phi}_i^n = \tfrac{1}{2}(\phi_i^{n+1} + \phi_i^{n-1}), \quad (23a)$$
$$\Delta x_{i+1/2} = (\Delta x_i + \Delta x_{i+1})/2, \quad (23b)$$
$$\Delta x_i = (\Delta x_{i+1/2} + \Delta x_{i-1/2})/2, \quad (23c)$$

where ϕ represents one of the physical variables such as ρ or ρu. The variable x represents one of the coordinates r or z, and $\Delta x_{i+1/2}(\Delta x_{j+1/2})$ is a space mesh interval between the grid point i (j) and $i+1$ $(j+1)$ in the radial (axial) direction. Equation (21) represents the centered difference and Eq. (22) represents the DuFort–Frankel scheme by which the time level of the diffusion term splits into the forward time level $n+1$ and the backward time level $n-1$ at the mid-grid in the centered space difference. These operators are applicable to the physical variables defined at the midplane of the cell. Similarly, if the subscript i is replaced by $i+1/2$, then the operators are applicable to those at the cell boundary.

As is mentioned before, our basic ideas are based on conservation laws, especially, the conservation of mass. For this reason, two time levels $n-1$ and $n+1$ are allowed for the space derivatives in the right-hand side of the mass conservation Eq. (14) corresponding to the leapfrog scheme. The explicit form of the equation evaluated at the backward time level $n-1$ is numerically unstable, whereas the implicit form is unconditionally stable. It follows, hence, that the mass is completely conserved for time and space by using the staggered grids and this implicit form. The convective terms in the energy equation are evaluated at the time level $n+1$ in order to be consistent with the mass conservation.

The algorithm is determined so as to solve explicitly the set of Eqs. (14)–(19) consistent with the implicit form of the mass conservation equation; the solution procedure takes the following form.

(1) Each value of mass velocity $(\rho u)^{n+1}$, $(\rho v)^{n+1}$ and $(\rho w)^{n+1}$ is independently computed from the values of the physical variables at the previous two time levels $n-1$ and n by use of momentum Eqs. (15)–(17).

(2) The density ρ^{n+1} is explicitly obtained by the substitution of $(\rho u)^{n+1}$ and $(\rho w)^{n+1}$ into the continuity Eq. (14) written in the implicit form.

(3) The pressure $(\rho T)^{n+1}$ is obtained similarly from the energy Eq. (18).

(4) The values of u^{n+1}, v^{n+1}, w^{n+1} and T^{n+1} are obtained by the division of the mass velocity and pressure by ρ^{n+1}.

(5) Steps (1)–(4) form a cycle when time proceeds a time mesh $\Delta\tau$.

(6) The following time filtering is made every m cycles to avoid computational splitting caused by the leapfrog scheme:

$$\phi^{n\pm 1/2} = (\phi^n + \phi^{n\pm 1})/2.$$

At the same time, time is dropped back $(1/2)\Delta\tau$.

(7) Steps (1)–(6) are repeated until the flow reaches the steady state.

4. Results

4.1. *Parameter Values for Computations*

Table II shows the parameter values used for the computations and the purpose of each case. These sets were chosen to clarify the effect of compressibility and nonlinearity. First, to observe the effect of compressibility, the thermally driven flows were computed for two cases of Mach numbers $M = 3.0$ and 4.0 because the effect appears more clearly in the thermally driven flow than in the mechanically driven flow. The Ekman number $E = 10^{-3}$ is chosen to take into account the effect of compressibility (i.e. Mach number). This value is not small enough to make the Ekman layer thin everywhere because the local Ekman number increases as the radius decreases. In particular, the region near the axis in the thermally driven flow

TABLE II

Computation Parameters

Case	Mach number M	Basic Flow	Purpose of analysis
1	3.0	Thermally driven flow	Effect of compressibility
2	4.0	Thermally driven flow	
3	4.0	Mechanically driven flow	Effect of dissipation heating and nonlinearity
4	4.0	Mechanically driven flow	

System: $E = 1.03 \times 10^{-3}$; $\gamma = 1.067$; $\sigma_p = 0.97$; $H/L = 1.0$; $\Delta T/T_0 = 3.125 \times 10^{-2}$.

becomes fully viscous for the case of $M = 4.0$. Secondly, it is of interest to study the procedure by which the high speed azimuthal flow is caused in the mechanically driven flow. Here, heating by viscous dissipation is taken into account in case 3, but not in case 4. The Mach number is held at $M = 4.0$. Furthermore, we examine whether or not our finite difference method is applicable to nonlinear problems such as in mechanically driven flow.

4.2. *Computational Details*

Figure 4 shows a resolution of 19×21 grid points arranged on the annulus with the aspect ratio of $A = 1.0$ and the inner radius of $r_a = 0.3$. The mesh intervals are nonuniform and uniform in the radial and the axial directions, respectively. This grid arrangement is determined by taking the boundary layer thickness into account; three or four grid points are induced within the boundary layer which is the $E^{1/3}$ layer on the vertical surface and the Ekman layer on the horizontal surface.

The time mesh is determined by both the numerical stability conditions derived from our finite difference scheme and the arrangement of the grid points. The upwind scheme used here is limited by the Courant–Friedrichs–Lewy (CFL) condition. Numerically, the velocity defined by the time and space meshes exceeds the characteristic velocity ΩL (i.e., $\Delta\tau < h$, where h is a minimum mesh interval in r or z directions). Physically, if $M > 1$, this condition also includes the time mesh restricted by the shock wave which propagates with the speed of sound (i.e., if $M > 1$, then $\Delta\tau < Mh$). The DuFort–Frankel leapfrog scheme is unconditionally stable for the arbitrary value of the time mesh about the purely diffusion equation. However, computational results of the thermally driven flow show that as the Mach number is increased, the solution converges until the time mesh becomes about 50 times as large as the time mesh limit of $\Delta\tau_e$ given by the Euler scheme; this relation is approximated by $\Delta\tau_e < (\Delta z)^2/4(E/\rho_e)$, where Δz is a minimum mesh interval in the z direction. It follows that the time mesh depends on the Mach number in the same relation $\Delta\tau \sim \rho_e(r_a)$ given by the Euler scheme because Δz is chosen as the Ekman layer thickness $E^{1/2}$, so that the time mesh is restricted by the lowest density near the axis of rotation. In the computations, the time iteration involved 7117 steps at

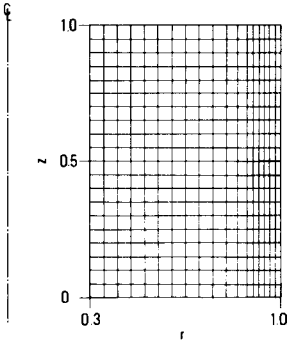

FIG. 4. A grid arrangement of 19×21.

$\Delta\tau = 5 \times 10^{-3}$ for case 1 (Table II) in which the time mesh ($\sim 20\Delta\tau_e$) is limited by the DuFort–Frankel scheme condition, and for case 2 in which the time mesh ($\sim h = 2 \times 10^{-2}$) is limited by the CFL condition. The time iteration involved 7117 steps at $\Delta\tau = 5 \times 10^{-3}$ for case 3 and 9150 steps at $\Delta\tau = 4 \times 10^{-3}$ for case 4. Note that both time meshes are also limited by the CFL condition, but the viscous dissipation aids in making the time mesh longer in case 3. When the number of time filterings was more than 50, the computation diverged due to time splitting caused by the leapfrog scheme. When the numbers were 20, 30 and 40, the computation converged, but the solutions differed slightly from each other. For this reason, time filtering was made every 30 time steps for all cases. The CPU time was of the order of 250 sec on a HITAC M-180 computer with IAP (Integrated Array Processor) using a core memory of 360K for a 19×21 resolution and 7117 steps. The CPU time depends on the total number N of the grid points in radial and axial directions, and also depends on the number N_t of the time iteration (i.e., the time up to the asymptotic state). If we take the spin-up time $E^{-1/2}$ defined at the outer sidewall as the measure of the time scale, $N_t = E^{-1/2}/\Delta\tau$ is written into $N^{1/2}/\rho_e(r_a)$ by using $E^{1/2} = \Delta z \sim N^{-1/2}$ and $\Delta\tau \sim \rho_e(r_a)$. If the time mesh is limited by the DuFort–Frankel scheme condition, the CPU time is proportional to $N^{1.5} \exp[1/2\gamma M^2(r_a^2 - 1)]$. Similarly, if the time mesh is limited by the CFL condition (i.e., $\Delta\tau < h$), the CPU time is proportional to N^2.

The enhanced stability of the upwind scheme over the centered space scheme of the convective term is a result of the introduction of the artificial viscosity (or numerical diffusion) term in the numerical procedure. The ratio of the artificial to real viscosity is approximated by $\alpha_r = 1/2(\rho w)\,\Delta r E^{-1}$ in the radial direction or by $\alpha_z = 1/2(\rho w)\,\Delta z E^{-1}$ in the axial direction using the same manner as in [22]. This indicates that the artificial viscosity is proportional to only the cell Reynolds number of Re ($= \rho u\,\Delta r E^{-1}$ or $\rho w\,\Delta z E^{-1}$) or proportional to both the grid size and the mass velocity. It should be noted that the artificial viscosity induced by the leapfrog and the upwind schemes does not depend on the Courant number c ($= u\,\Delta\tau/\Delta r$ or $w\,\Delta\tau/\Delta z$) which appears in that induced by the Euler and the upwind schemes (i.e., $\alpha = 1/2\,\mathrm{Re}(1 - c)$). Table III shows the maximum values and their positions of artificial viscosity resulting from all cases. It can be seen that the artificial viscosity is

TABLE III

Maximum Values of the Artificial Viscosity

Case	Artificial viscosity in the radial direction α_r	Coordinates r	z	Artificial viscosity in the axial direction α_z	Coordinates r	z
1	9.28×10^{-3}	0.92	0.025	4.15×10^{-2}	0.92	0.50
2	2.19×10^{-4}	0.94	0.025	1.51×10^{-2}	0.97	0.50
3	9.99×10^{-3}	0.87	0.075	3.20×10^{-1}	0.97	0.25
4	1.02×10^{-2}	0.87	0.075	3.19×10^{-1}	0.97	0.20

small in comparison with the real viscosity. Although the artificial viscosity in the axial direction seems large for the mechanically driven flow, the effect is small; the computation using a 19×21 resolution shows that the axial velocity changes slightly in comparison with those by a finer 24×26 and a coarser 14×16 resolution (see Appendix).

The DuFort–Frankel leapfrog scheme introduces the artificial wave during the transient state, but this effect becomes small when we choose an adequate time mesh and grid size. The results of such tests mentioned above are discussed in the Appendix (see Fig. 12).

4.3. *Evolution of the Flow*

The time development of the flow is illustrated by kinetic energies and the average temperature in Figs. 5a and b for cases 2 (thermally driven flow) and 3 (mechanically driven flow), respectively. The transient aspects of cases 2 and 3 are similar to the

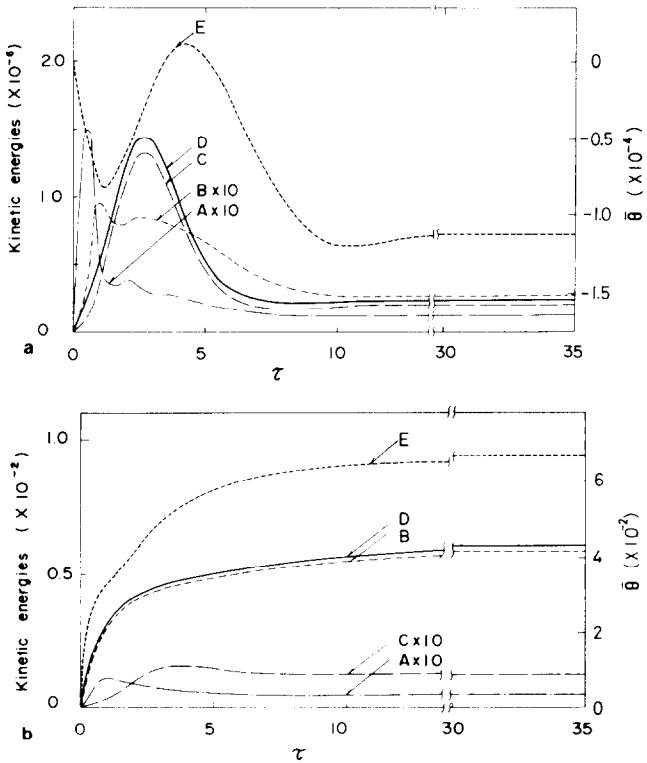

FIG. 5. Time development of kinetic energies and average temperature for (a) case 2 (thermally driven flow) and (b) case 3 (mechanically driven flow). Diagrams have global integrals; (A) $\langle \frac{1}{2}\rho u^2 \rangle$; (B) $\langle \frac{1}{2}\rho v^2 \rangle$; (C) $\langle \frac{1}{2}\rho w^2 \rangle$; (D) $\langle \frac{1}{2}\rho(u^2 + v^2 + w^2) \rangle$; (E) $\bar{\theta}$.

We can see that the thermally driven flow is predominantly an axial flow at all times resulting from the Taylor–Proudman theorem [24] as shown in Fig. 5a. The transient states are similar to those discussed in [15, 25] except the compressibility effect; these time scales are formation times of the Ekman layer, the $E^{1/3}$ layer and the spin-up time. The formation of the Ekman layer is shown by the result that both radial and azimuthal components of mean kinetic energy increase and decrease to each other during the initial stage of $\tau = 0 - 3$ ($\sim O(1)$) with the oscillation (whose frequency is about 2Ω [26]) caused by the Coriolis force. The spin-up process is also shown by the result that the axial component increases gradually. Hereafter, all of them approach the steady state and tend to be steady at $\tau \sim 10$ when the $E^{1/3}$ layer is formed. This suggests that the spin-up time ($\sim O((E/\rho)^{-1/2})$) is of the same order as the formation time ($\sim O((E/\rho)^{-1/3})$) of the $E^{1/3}$ layer due to compressibility effects. In fact, computational results show that the maximum value of the axial velocity (at the position of $r = 0.725$ and $z = 0.50$) reaches 93.1, 99.8 and 100.0% of the steady state value at times $\tau = 10$, 20 and 30, respectively. No variation was observed within four significant figures of the computed values during $\tau = 30 - 35$, and hence the steady state is represented by the asymptotic solution at $\tau = 35$.

As seen in Fig. 5b, on the other hand, the kinetic energy of the mechanically driven flow is about 10^4 times as large as that of the thermally driven flow due to the azimuthal velocity difference between both cases; the azimuthal velocity is of order unity (i.e., $\sim \Omega L$ in the dimensional unit) for the mechanically driven flow and it is on the order of $\Delta T/T_0 = 3.125 \times 10^{-2}$ (i.e., $\sim (\Delta T/T_0)\,\Omega L$) for the thermally driven flow. Furthermore, the azimuthal component of the mean kinetic energy plays a primary role at all times for the mechanically driven flow. The azimuthal component rapidly increases (in a rotating system, but it decreases in an inertial system) during the initial stage of $\tau = 0 - 3$, and hereafter it approaches the steady state monotonically. Both radial and axial components reach the maximum values at $\tau = 1$ and 3, respectively, after the initial increase, and they decrease while approaching the steady state. The convergence rate in case 3 is similar to that in case 2 and the steady state is represented by the asymptotic solution at $\tau = 35$. Cases 1 and 4 also converged at $\tau = 35$.

The time variation of the average temperature $\bar{\theta}$ is very similar to that of $\langle \frac{1}{2}\rho w^2 \rangle$ due to the compression (or expansion) work for the thermally driven flow. For the mechanically driven flow, the variation of $\bar{\theta}$ corresponds to that of $\langle \frac{1}{2}\rho v^2 \rangle$ due to the dissipation heating.

4.4. *Thermally Driven Flow*

Before comparing our results with those of the boundary layer theory [5, 6], we summarize the results of the theory. The theory predicts that the Ekman layers and the $E^{1/3}$ layer [12] are formed on end plates and on the sidewall of the cylinder (not an annulus), respectively, and that there are two main circulations associated with these horizontal and vertical boundary layers. One is the Ekman suction flow in the inviscid core from the top to the bottom. The flow within the $E^{1/3}$ layer is circulating in the same direction as the Ekman suction flow. These boundary layers match the

thermal wind in the inviscid core with the boundary conditions imposed on the surface.

The computational conditions of case 1 ($M = 3.0$) are within the assumption of the boundary layer theory except for the geometrical configuration used in our computations. The computational conditions of case 2 ($M = 4.0$) is beyond the assumption of the theory by virtue the absence of the inviscid core caused by the compressibility effect.

Results of cases 1 ($M = 3.0$) and 2 ($M = 4.0$) are shown in Figs. 6 through 9 at the time $\tau = 35.0$ when the solution becomes almost steady. Figures 6a and b show the vector plots of the meridional motion for cases 1 and 2, respectively. We can observe that the thermally driven circulation is established for both cases and that the circulation is almost axial as is predicted by the partition of the kinetic energy. Secondly, the flow pattern does not change although the circulation is weakened as the Mach number is increased. These results suggest that the prediction of the boundary layer theory qualitatively agrees with the present results for the strongly compressible, viscous case of $M = 4.0$.

Figure 7 shows the contour plots of the azimuthal velocity plotted with the same intervals. We can see that the thermal wind, however, becomes weaker as the Mach number is increased corresponding to the weakness of the circulation. The structure of the thermal wind is asymmetric with respect to the midheight $z = 0.50$. The asymmetric structure is confirmed by the axial distributions of the azimuthal velocity for the case of $M = 4.0$ shown in Fig. 9b. Corresponding to this asymmetry, the axial distributions of the radial velocity in Fig. 9a are also asymmetric with respect to $z = 0.50$ at both radii $r = 0.5$ and 0.7. The profile at $r = 0.9$ shows that the radial flow is confined near the top and the bottom plates by the smallness of the local Ekman number (cf. Fig. 11a).

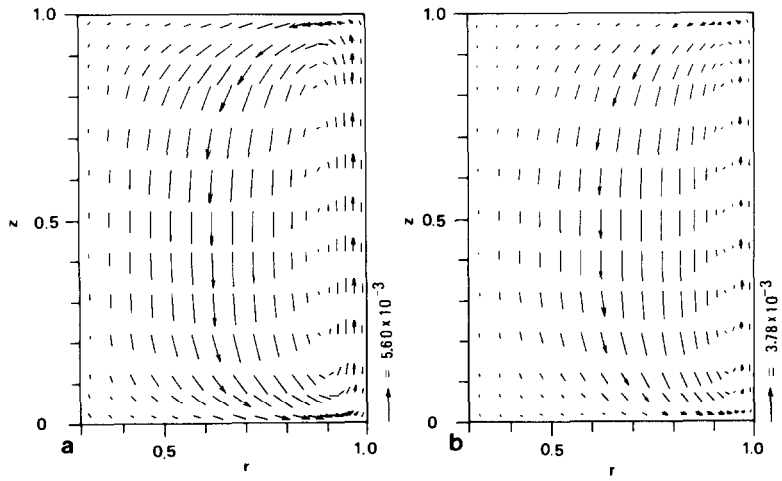

FIG. 6. Vector plots of the meridional motion at $\tau = 35.0$ for the thermally driven flow with (a) $M = 3.0$ (case 1) and (b) $M = 4.0$ (case 2).

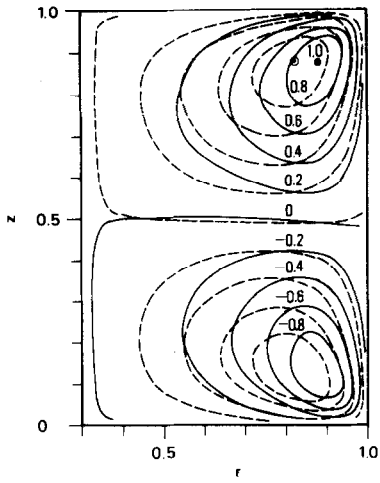

FIG. 7. Contour plots of the azimuthal velocity at $\tau = 35.0$; (– – –) $M = 3.0$ (case 1), where maximum ($\odot$) $= 6.01 \times 10^{-3}$; (——) $M = 4.0$ (case 2), where maximum (●) $= 9.85 \times 10^{-3}$.

The contour plots of temperature (isotherms) are shown in Fig. 8. We see that the isotherms are approximately parallel to the end plates and are nearly equidistant to each other, except near the inner cylinder (i.e., most of the gas has nearly the same temperature as the outer cylinder on which the temperature is a linear function of z). The contour 0, which represents the average temperature of both plates, is located at the midheight $z = 0.50$. This is related to the asymmetric structure of the thermal wind. The isotherms vary slightly with the variation of the compressibility. The temperature approaches more to that of the outer cylinder for $M = 4.0$ than for

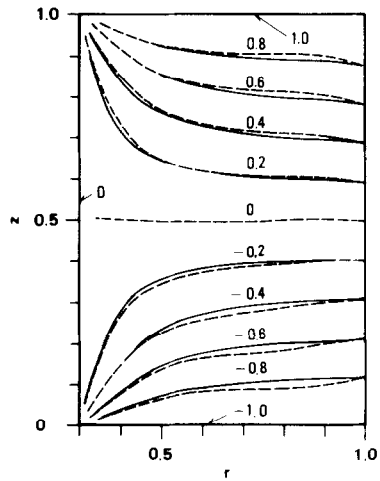

FIG. 8. Contour plots of temperature (isotherms); (– – –) $M = 3.0$ (case 1); (——) $M = 4.0$ (case 2). Values are scaled by $\Delta T/T_0 = 3.125 \times 10^{-2}$.

$M = 3.0$. This is because the thermal diffusivity is increased as the compressibility is increased by the fact that the density rapidly decreases towards the inner cylinder.

Finally, we make a quantitative comparison of our results with the boundary layer approximation. Figure 9c shows the radial distributions of the axial velocity at the midheight $z = 0.50$. The analytic solution is only for $M = 3.0$ because the boundary layer is not applicable for the case of $M = 4.0$. For the present comparison, the result of case 1 ($M = 3.0$) is scaled by the characteristic velocity of case 2 ($M = 4.0$). It is interesting that the maximum value of the axial velocity is on the same order of the Ekman suction flow despite the different geometry (the cylinder and the annulus) and temperature. This implies that the Ekman suction flow is established in the region near the end plates. We see that the $E^{1/3}$ layer solution disagrees with the result of case 1 ($M = 3.0$), i.e., the axial velocity near the outer cylinder is larger than that of the $E^{1/3}$ layer solution and the layer is thinner than that predicted by the $E^{1/3}$ layer

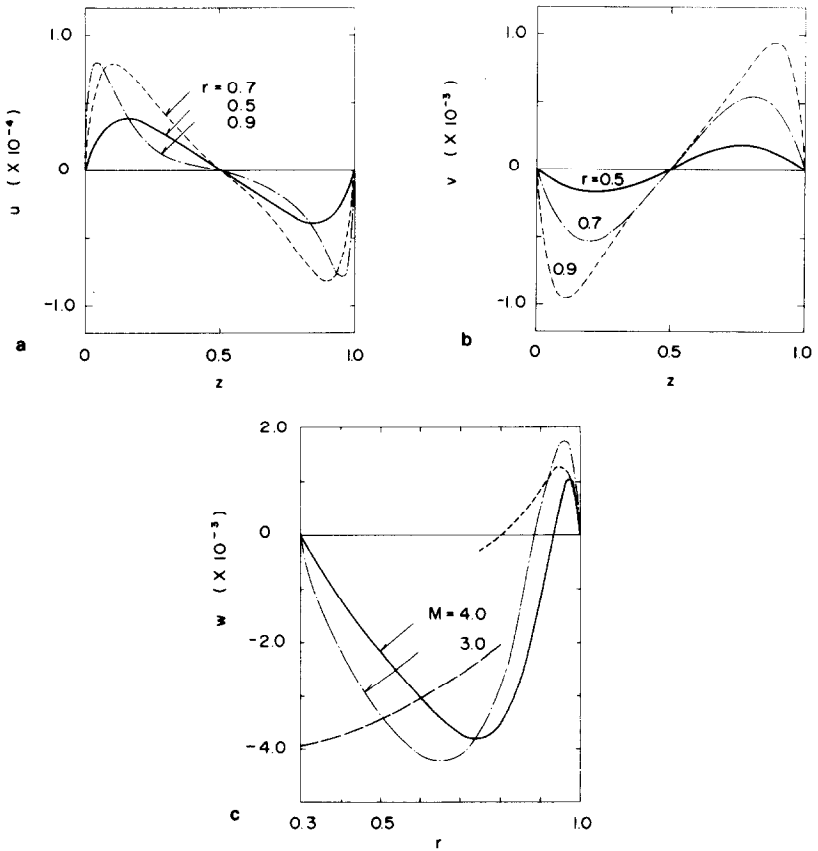

FIG. 9. Results of case 2 (thermally driven flow) at $\tau = 35.0$. (a) The vertical profiles of the radial velocity. (b) The vertical profiles of the azimuthal velocity. (c) The horizontal profiles of the axial velocity at $z = 0.50$. Figure 9c includes results of case 1 ($M = 3.0$) and the boundary layer analysis (– – –, $E^{1/3}$ layer solution; – · –, Ekman suction solution) for $M = 3.0$ for comparison.

solution. As a result in case 2 ($M = 4.0$), the axial velocity is decreased and the profile moves towards the outer cylinder. This suggests, as we expected, that the amount of the circulating mass becomes weak as compressibility is increased. At the same time, the role of the Ekman layer suction becomes small in the mass transport by the increases of the kinematic viscosity in the low density interior.

4.5. *Mechanically Driven Flow*

The mechanically driven flow caused by the scoop pipe is approximated by the slowly rotating plate under the assumption of axisymmetry [1]. Physically, the present case provides us with the limiting case of the mechanically driven flow because the large angular velocity difference is imposed on the annulus as shown in Fig. 2b. For this reason, the present case also provides us with an opportunity to examine whether or not our finite difference technique is applicable to the nonlinear problem. In addition, the mechanical energy is transformed into heat both by molecular dissipation (friction) and by compression (or expansion) work. Cases 3 and 4, respectively, are computed with and without molecular disipation to examine its effect.

Results of cases 3 and 4 are shown in Figs. 10 and 11 at time $\tau = 35.0$ when the asymptotic behaviour of our solution represents the steady state (see Section 4.3). Figure 11a shows the radial distributions of the local Ekman number at $z = 0.50$. Results of the thermally driven flows are also given for comparison. The local Ekman number rapidly increases towards the axis of rotation because the angular velocity is nearly equal to that of the rigid body rotation. Particularly, the local Ekman number exceeds the order unity near the inner cylinder for $M = 4.0$ (case 2). On the other hand, the increase of the local Ekman number is gradual for the mechanically driven flow because of the slower rotation compared with the rigid body rotation. It follows, hence, that the thermally driven flow for $M = 4.0$ is effectively more viscous than the mechanically driven flow. Figures 10a and b, respectively, show the velocity vector plots of the meridional motion and contour plots of the azimuthal velocity plotted with the same intervals, for case 3. We see that the countercurrent flow circulates from the bottom to the top plate near the outer cylinder. It is noted that the flow pattern is quite different from that of the thermally driven flow (case 2), i.e., the thermally driven flow is stretched along the direction of the axis of rotation and the stretch is weaked in the case of the mechanically driven flow (Fig. 6b). We see that most of the gas rotates faster than half the angular velocity of the outer cylinder, and that the region of the low azimuthal velocity is confined in the neighbourhood of the bottom stationary plate. This is because the angular momentum given from the rotating surface is larger than that taken from the stationary surface. As we see in Fig. 11c, the radial distributions of the angular velocity are smaller than that of the cylindrical Couette flow because of the presence of the bottom stationary plate. Axial distributions of the angular velocity are larger than that of the flow between a stationary and a rotating infinite disk [27] as Fig. 11d shows, because the angular velocity is increased by the outer rotating cylinder. The axial distribution of the

angular velocity induces the vertical density stratification in which the upper region is effectively more viscous than the lower region. A strong radial inflow is formed in the bottom Ekman layer (which becomes thicker towards the inner cylinder) as is shown in Fig. 11b. The meridional flow becomes weak and wide, and changes its direction towards the outer cylinder as it approaches the upper region, where the flow field is more viscous than the lower region (Fig. 10a).

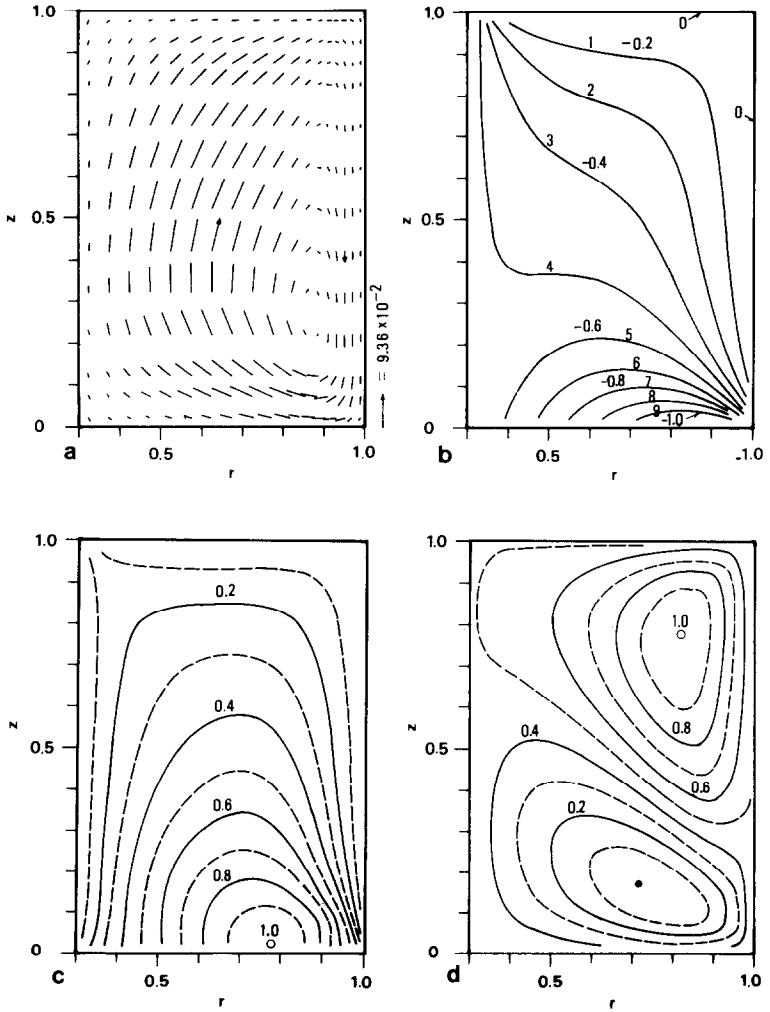

FIG. 10. Results of cases 3 and 4 (mechanically driven flow) at $\tau = 35.0$. (a) Vector plots of the meridional motion. (b) Contour plots of the azimuthal velocity, where contour 9 represents the value of -7.13×10^{-1}. (c) Contour plots of temperature (isotherms) where maximum (○) = 1.19. (d) Contour plots of temperature (isotherms) for case 4, where maximum (○) = 1.01 and minimum (●) = 9.89×10^{-1}.

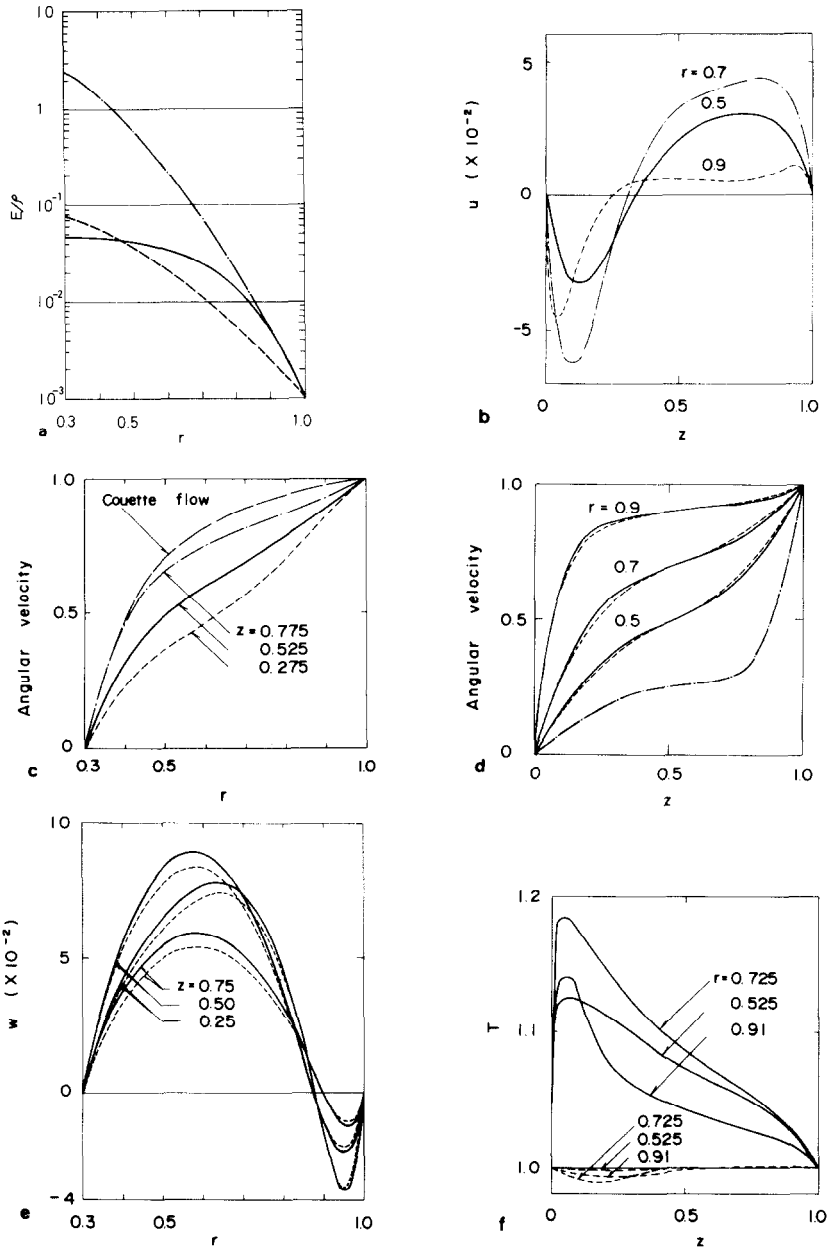

FIG. 11. Results of cases 3 and 4 at time $\tau = 35.0$. (a) The radial distribution of the local Ekman numbers at $z = 0.50$; (– – –) $M = 3.0$ (case 1); (– · –) $M = 4.0$ (case 2); (——) case 3. (b) The horizontal profiles of the radial velocity for case 3. (c) The horizontal profiles of the angular velocity for case 3. (d) The vertical profiles of the angular velocity; (——) case 3; (– – –) case 4; (– · –) $E = 10^{-2}$ (Pearson [27]). (e) The horizontal profiles of the axial velocity; (——) case 3; (– – –) case 4. (f) The vertical profiles of temperature; (——) case 3, (– – –) case 4.

When dissipation is absent (i.e., for case 4), the mechanically driven flow becomes weak although the flow pattern varies only slightly. Figure 11e clarifies that the axial velocity is decreased by the absence of dissipation. It should be noted that when dissipation is absent, the angular velocity is decreased in the lower region ($z < 0.50$) of low temperatures by the expansion work and is increased in the upper region ($z > 0.50$) of high temperatures by the compression work. To the contrary, when dissipation is present, the thermal wind is induced by the axial temperature gradient. Hence, the mechanically driven flow becomes stronger by coupling with the thermally driven flow which is caused by the dissipation heating.

Figure 10c shows contour plots of the temperature (isotherms) plotted with the same interval. Isotherms indicate that the temperature increases steeply near the bottom plate and decreases near the top plate despite no prescribed temperature difference on the boundary. In particular it reaches the maximum value near the bottom plate corresponding to the location of the minimum value of the angular velocity (Fig. 10b). The temperature field depends on the gas motion by the effect of the dissipation and the compression (or expansion) work. In case 3, the azimuthal component is the major part of total kinetic energy as we can see in Fig. 5b. Hence heating by compression or cooling by expansion is small in comparison with heating by friction. This is because the Eckert number $E_c = (\gamma - 1) M^2$ and the relative difference of the azimuthal velocity between the gas and the annulus are both on the order of unity. Figure 10d shows the contour plots of the temperature (isotherms) for the case without dissipation (case 4). We see that the temperature decreases near the bottom plate by expansion and it increases near the top plate by compression. Axial distributions of the temperature are shown in Fig. 11f including both cases with and without dissipation. These results clarify that the dissipation heating is more important than the heating by compression (or expansion) for the mechanically driven flow.

5. Conclusion

We have presented a finite difference method for solving the full Navier–Stokes equations of a compressible, rotating gas. This method, based on the upwind and DuFort–Frankel schemes, is efficient for computations of strongly compressible rotating flows. The method is applied to the thermally and mechanically driven flow in a gas centrifuge in order to examine our finite difference method.

Computations provide us with reasonable results for both flows. It is found that the thermally driven circulation becomes weak as the effect of compressibility increases. In the mechanically driven circulation, the temperature increases by viscous dissipation despite the cooling by expansion work and the lack of temperature difference on the boundary.

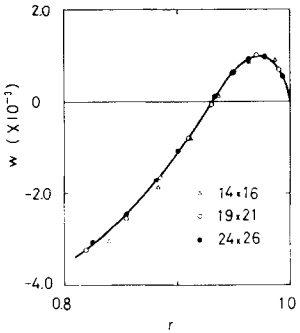

FIG. 12. Comparison of the axial velocity results at $z = 0.50$ for a 14×16, a 19×21 and a 24×26 resolution of case 2 (thermally driven flow for $M = 4.0$).

APPENDIX

The computational results include the errors of meshes for time and space associated with the present finite difference schemes, so that computations are carried out with variations of time and space meshes in order to examine the accuracy of computaions. The 14×16 and 24×26 resolutions, respectively, are chosen as the rough and dense grid systems in order to compare the results from a 19×21 resolution using the fixed time mesh $\Delta\tau = 5 \times 10^{-3}$. A smaller time mesh $\Delta\tau = 4 \times 10^{-3}$ is chosen to compare with results from the time mesh $\Delta\tau = 5 \times 10^{-3}$ with the fixed 19×21 resolution. Figure 12 shows the horizontal profiles of the axial velocity at midheight $z = 0.50$ for case 2 (thermally driven flow) using 14×16, 19×21 and 24×26 resolutions. In comparison with these results, the axial velocity is decreased by about 3% for the dense grid resolution and is increased by about 4% for the rough grid resolution. Other physical variables change very slightly for both resolutions. Results change more slightly for the time mesh variation than those for the space mesh variation. Similar results are obtained for the mechanically driven flow with respect to the variations of time and space meshes.

ACKNOWLEDGMENTS

The author is grateful to Professor Takeo Sakurai of Kyoto University for reading the manuscript. The author is also grateful to continuing encouragement from Drs. K. Taniguchi, S. Yamada, A. Doi and N. Ozaki of the Energy Research Laboratory.

REFERENCES

1. D. R. OLANDER, *Sci. American* **239** (1978), 27.
2. D. R. OLANDER, *in* "Advances in Nuclear Science and Technology," Vol. 6, p. 104, Academic

3. SOUBBARAMAYER, *in* "Proceedings, Second Workshop on Gases in Strong Rotation" (Soubbaramayer, Ed.), CEN, Saclay, 1977.
4. E. RATZ, "Aerodynamic Separation of Gases and Isotopes," Lecture Series 1978–8, Von Kármán Institute for Fluid Dynamics, 1978.
5. T. SAKURAI AND T. MATSUDA, *J. Fluid Mech.* **62** (1974), 727.
6. W. NAKAYAMA AND S. USUI, *J. Nucl. Sci. Tech.* **11** (1974), 242.
7. H. MIKAMI, *J. Nucl. Sci. Tech.* **10** (1973), 369.
8. T. MATSUDA AND K. HASHIMOTO, *J. Fluid Mech.* **73** (1976), 389.
9. T. MATSUDA AND K. HASHIMOTO, *J. Fluid Mech.* **78** (1976), 337.
10. T. MATSUDA AND K. HASHIMOTO, *J. Fluid Mech.* **85** (1978), 433.
11. T. MATSUDA AND H. TAKEDA, *J. Fluid Mech.* **85** (1978), 443.
12. K. STEWARTSON, *J. Fluid Mech.* **3** (1957), 17.
13. V. BARCILON AND J. PEDLOSKY, *J. Fluid Mech.* **29** (1967), 673.
14. G. M. HOMSY AND J. L. HUDSON, *J. Fluid Mech.* **35** (1967), 33.
15. I. HARADA AND N. OZAKI, "Lecture Notes in Physics," No. 35, p. 197, Springer–Verlag, Berlin, 1975.
16. E. JUNG, DFVLR-Kolloquium, Protz-Wahn, 143, 1970.
17. S. LOPEZ, *in* "Proceedings, EUROMECH-Colloquium-80, Karlsruhe" (K. G. Roesner, Ed.), p. 43, 1977.
18. T. KAI, *in* "Proceedings, Second Workshop on Gases in Strong Rotation" (Soubbaramayer, Ed.), p. 231, CEN, Saclay, 1977.
19. SOUBBARAMAYER AND J. P. LAHARGUE, *in* "Proceedings, Second Workshop on Gases in Strong Rotation" (Soubbarameyer, Ed.), p. 193, 1977.
20. P. J. ROACHE, "Computational Fluid Dynamics," Hermosa, Albuquerque, 1972.
21. R. A. GENTRY, R. E. MARTIN, AND B. J. DALY, *J. Comput. Phys.* **1** (1966), 87.
22. P. J. ROACHE, *J. Comput. Phys.* **10** (1972), 169.
23. G. VERONIS, *Tellus* **19** (1967), 326.
24. H. P. GREENSPAN, "The Theory of Rotating Fluids," Cambridge Univ. Press, London/New York, 1968.
25. I. HARADA AND N. OZAKI, *J. Phys. Soc. Japan* **45** (1978), 1400.
26. I. HARADA, *J. Phys. Soc. Japan* **47** (1979), 1313.
27. C. E. PEARSON, *J. Fluid Mech.* **21** (1965), 623.